CrossMark

JM PAPERS

Morphology of oblique detonation waves in a stoichiometric hydrogen–air mixture

Honghui Teng[1], Cheng Tian[1], Yining Zhang[2], Lin Zhou[1,2],† and Hoi Dick Ng[3]

[1]School of Aerospace Engineering, Beijing Institute of Technology, Beijing 100081, PR China

[2]State Key Laboratory of Laser Propulsion and Application, Beijing Power Machinery Institute, Beijing 100074, PR China

[3]Department of Mechanical, Industrial and Aerospace Engineering, Concordia University, Montreal, QC H3G 1M8, Canada

Although the morphology of oblique detonation waves (ODWs) has been widely studied, it remains impossible to predict the wave systems in the initiation region, which is a critical component in promoting engine applications. Such wave systems are usually viewed as secondary ODWs or compression waves (CWs), introducing some structural ambiguities and contradictions with recent observations. In this study, ODWs are simulated numerically in a stoichiometric hydrogen–air mixture and their morphological features are analysed. To cover a wide range of flight conditions physically, the control parameters are the flight altitude H_0 and Mach number M_1 of an ODW-based engine. Numerical results reveal the morphological variations with respect to H_0 and M_1, within which two special wave systems arise. One wave system indicates that the CW might induce an abrupt transition, and the other indicates that the classical secondary ODW might evolve into a normal detonation wave, another illustration of the well-known 'detonation-behind-shock' wave configurations. To clarify the mechanism of wave system variation, a geometric analysis of two characteristic heights demonstrates that the wave system could be predicted from the viewpoint of CW convergence. Moreover, analysis of the induction zone Mach number, compared with the corresponding Chapman–Jouguet Mach number, provides a criterion for the normal detonation wave formation. These semi-theoretical approaches collectively enhance our understanding of the wave system physically.

Key words: detonation waves

† Email address for correspondence: linxzhou@foxmail.com

H. Teng, C. Tian, Y. Zhang, L. Zhou and H.D. Ng

1. Introduction

There are two types of detonation waves, normal and oblique, depending on whether the pre-shock inflow is perpendicular or not to the detonation surface. Benefiting from high thermal efficiency and fast heat release, oblique detonation waves (ODWs) have the potential to be used in air-breathing hypersonic engines. Compared with traditional Scramjets (supersonic combustion ramjet), ODW-based engines have several theoretical advantages, such as their high specific pulse and reduced size (Wolański 2013). To harness the ODW within supersonic inflows, it is first necessary to clarify the morphology of ODWs. In early works, e.g. Pratt, Humphrey & Glenn (1991), ODWs were treated as oblique shock waves (OSWs) with instant heat release. This model was soon found to be oversimplified: numerical (Li, Kailasanath & Oran 1994) and experimental (Viguier, Gourara & Desbordes 1996) studies observed the coexistence of an initiation region and a well-established ODW with finite heat release layer. These findings inspired later studies that revealed many different ODW structures. However, the connections and boundaries of these structures have not been quantitatively studied, and it remains impossible to predict precisely the morphology of ODWs.

Morphological studies of ODWs focus on three aspects, namely the OSW–ODW transition, the ODW surface instability and the wave system of the reactive front in the initiation region. Regarding the first aspect, two OSW–ODW transition types have been observed, named the smooth transition and the abrupt transition. The former is achieved by a curved section of the shock, whereas the latter is formed by an abrupt multi-wave point. The transition type is dependent on various parameters, such as the inflow Mach number, and several criteria have been proposed (Teng & Jiang 2012; Miao *et al.* 2018). In terms of the ODW surface instability, the destabilization processes have been examined and found to be sensitive to the overdriven degree and activation energy (Teng, Jiang & Ng 2014; Teng *et al.* 2015; Zhang *et al.* 2018). More recently, the effects of unsteady inflow have been simulated, demonstrating a novel destabilization mechanism triggered by an extraneous source (Yang, Ng & Teng 2019*a*). Our latest study of ODW dynamics also considered a more complex engine geometry by investigating the influence of a far-field upper expansion corner. A special wave complex featuring a recirculation zone is revealed due to the flow–wall interaction and ODW decoupling. The enhanced surface instability from the interaction is also shown to induce destabilization of the ODW structure (Wang *et al.* 2020). However, the third aspect, namely the wave system of the reactive front in the initiation region, has not yet been investigated in detail. For simplicity, the wave system is described as either one oblique shock, such as in Ghorbanian & Sterling (1996), or one compression wave (CW) (Li *et al.* 1994). Coupled with the reactive front, the former leads to an ODW, usually named the secondary ODW (SODW), whereas the latter leads to a deflagration wave. Recently, a fuel mixture (Ar-diluted C_2H_2–O_2) was used to study the ODW morphology, illustrating that the wave systems have some new forms beyond the simple CW or SODW (Fang *et al.* 2019*a*; Zhang *et al.* 2019). These results indicate that the wave systems are more complicated than the two classical forms suggest, so it is necessary to investigate their morphology. In essence, the wave system is critical in achieving a fundamental understanding of the morphology of ODWs, as it not only affects the OSW–ODW transition but may also change the surface instability (Yang *et al.* 2019*b*).

This study describes a series of simulations and analyses of ODW morphology, especially the wave systems. Based on the most widely used fuel, i.e. stoichiometric hydrogen–air, a parameter-selection method that is different from that of most previous studies is employed. The controlling parameters are chosen to be the flight altitude H_0 and Mach number M_1 of an ODW-based engine, rather than the widely used parameters of the

pre-detonation mixtures. Hence, the parameters are not artificial, but are related to realistic flight conditions (although the fuel–air mixing is ignored at this stage), and could vary over a wide physical range. The simulation results not only reveal morphological variations that depend on H_0 and M_1, but also demonstrate the existence of two special wave systems. A semi-theoretical approach to the morphology of ODWs is developed by combining two analysis methods, allowing us to clarify the mechanisms of the different wave systems. While conventional wisdom approaches this type of problem in an analytic fashion using shock polar analysis, such as investigations of condensed-phase detonation interaction with confinement (e.g. Short & Quirk 2018; Bdzil, Short & Chiquete 2020), many simplifying assumptions are unavoidably required (Powers & Stewart 1992). The analytical results may not always reflect the numerically observed flow pattern in certain cases (Short & Quirk 2018), particularly for a finite-length reaction-zone detonation. Indeed, the finite reaction and complex wave interactions in the initiation zone make a tractable analytic formalism challenging if not impossible. Numerical simulations remain a widely applied technique for tackling such complex phenomena of interaction between gas dynamics and finite heat release in the initiation region and identify possible wave systems with realistic conditions.

2. Physical model and computational method

Schematics of the ODW-based engine considered in this paper and the wedge-induced ODW are shown in figure 1. Following the engine inlet configuration proposed by Dudebout, Sislian & Oppitz (1998) and adopted in later research (Sislian *et al.* 2001), the high-altitude air inflow is assumed to be compressed by two equal-strength oblique shock waves. This inlet condition ensures the same ratio of pressure or temperature across the shock. Different from equal-deflection angle employed before (Wang *et al.* 2015), this inlet wave configuration could minimize the entropy increase, which is critical for improving propulsion performance. The fuel and air are also assumed to be well premixed at the inlet and the effect of injection is not considered. In fact, the injection of fuel in the supersonic inflow can lead to complicated cases (Ren *et al.* 2019*a*), and this process determining whether the mixture could be well premixed could affect significantly the ODW initiation. Since the flow of the incoming air is supersonic, efficient premixing with fuel in the inlet is inevitably difficult to achieve, resulting in an inhomogeneous mixture (Iwata, Nakaya & Tsue 2017). Nonetheless, for the Mach number range considered in this investigation, the mixing length and ignition requirement are less severe (Menees, Adelman & Cambier 1991), and in another research context, several injector design concepts (e.g. strut type, etc.) of providing almost complete premixing of fuel with air at supersonic speeds have been proposed and analysed in a number of studies (Cambier, Adelman & Menees 1990; Menees *et al.* 1991; Valorani, Di Giacinto & Buongiorno 2001; Alexander, Sislian & Parent 2006). For liquid fuels, the complexity of multiphase flows presents also another hurdle (Ren *et al.* 2018, 2019*b*). Considering that there are several multi-physics affected by a number of gas-dynamic and geometric parameters, which is hard to be determined because there are no referential engines so far, the injection process is thus not modelled here. In the early stage of engineering design, a coefficient of total pressure recovery is usually introduced to model the injection effects, but we try to avoid any artificial parameters and focus on the fundamental phenomena, so also not utilized here. In the present set-up, the premixed combustible supersonic inflow thus reflects on the two-dimensional wedge and first generates an OSW. The high post-shock temperature may trigger exothermic chemical reactions and subsequently induce ODW initiation downstream. In this study, the computational domain is enclosed by the dashed line in figure 1, whose coordinates
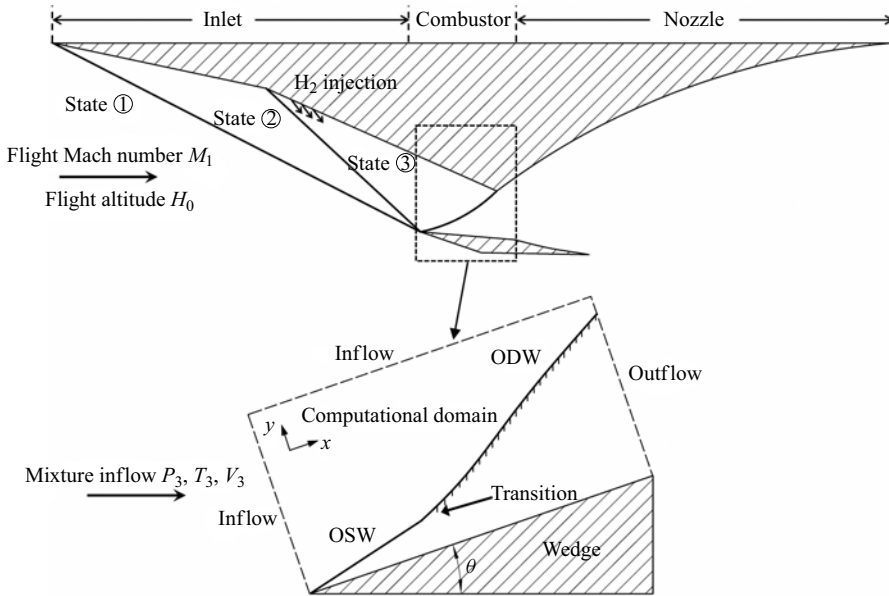
Figure 1. Schematics of an ODW-based engine and the wedge-induced ODW computational domain.

are rotated to the direction along the wedge surface. Hence, the Cartesian grid in the rectangular domain is aligned with the wedge surface.

Viscous effects are thought to be negligible because the Reynolds number is very high (Li, Kailasanath & Oran 1993; Figueira da Silva & Deshaies 2000). Many previous numerical studies (Sislian *et al.* 2001; Choi *et al.* 2007; Choi, Shin & Jeung 2009; Verreault, Higgins & Stowe 2013; Liu *et al.* 2015; Wang *et al.* 2015; Yang *et al.* 2019*a*) are thus based on an inviscid assumption. Recent studies, such as those of Fang, Zhang & Hu (2019*b*) and Li *et al.* (2020), also demonstrate that the boundary layer may change the ODW structures only in certain circumstances and has a limited impact on the main flow region downstream of the ODW. More recent studies, such as that of Laguarda *et al.* (2020), show that the inviscid flow model can still provide insight into the dynamics of unsteady shock interactions with moving wedges from a high-Mach-number flow. Despite the fact that a recirculation zone could affect the flow at the vicinity of the wall, creating certain unsteadiness and changing the location of initiation point, the type of global wave configuration remains unaffected. Therefore, this study still employs the inviscid assumption to be consistent with most previous studies, focusing primarily on the shock and heat release interaction. In addition, the role of physical diffusion is not considered in this work, although such an effect needs careful attention if highly unstable detonations, for example in methane–air mixtures, are considered of which the turbulent nature of the front provides another ingredient in the detonation propagation mechanism (Radulescu 2018). In this investigation, the governing equations are thus simplified to the two-dimensional, multi-species Euler equations given by

$$\frac{\partial \boldsymbol{U}}{\partial t} + \frac{\partial \boldsymbol{F}}{\partial x} + \frac{\partial \boldsymbol{G}}{\partial y} = \boldsymbol{S}, \qquad (2.1)$$

where

$$
\boldsymbol{U} = \begin{bmatrix} \rho_1 \\ \vdots \\ \rho_n \\ \rho u \\ \rho v \\ e \end{bmatrix}, \quad \boldsymbol{F} = \begin{bmatrix} \rho_1 u \\ \vdots \\ \rho_n u \\ \rho u^2 + P \\ \rho u v \\ (e+P)u \end{bmatrix}, \quad \boldsymbol{G} = \begin{bmatrix} \rho_1 v \\ \vdots \\ \rho_n v \\ \rho u v \\ \rho v^2 + P \\ (e+P)v \end{bmatrix}, \quad \boldsymbol{S} = \begin{bmatrix} \dot{\omega}_1 \\ \vdots \\ \dot{\omega}_n \\ 0 \\ 0 \\ 0 \end{bmatrix}. \quad (2.2a\text{--}d)
$$

Here, ρ, u, v and P represent the density, velocity along the x-axis direction, velocity along the y-axis direction and pressure, respectively. The density ρ and total energy e are calculated by

$$
\rho = \sum_{i=1}^{n} \rho_i, \tag{2.3}
$$

$$
e = \rho h - P + \tfrac{1}{2}\rho(u^2 + v^2), \tag{2.4}
$$

where the specific enthalpy can be written as $h = \sum_{i=1}^{n} \rho_i h_i / \rho$ with h_i obtained from the thermodynamic data of each species. The equation of state is

$$
P = \sum_{i=1}^{n} \rho_i \frac{R_0}{w_i} T, \tag{2.5}
$$

where w_i is the molecular weight, T is the gas temperature, R_0 is the universal gas constant and $\dot{\omega}_i$ is the species' specific mass production rate, dictated by the chemical reaction model. The chemical kinetic model used in this study is one of the most recent, comprehensive H_2/O_2 kinetic mechanisms suitable for high-pressure combustion (Burke *et al.* 2012). This mechanism involves 27 reversible, elementary reactions among eight species (H_2, O_2, H_2O, H, O, OH, HO_2 and H_2O_2) with five inert species (N_2, Ar, He, CO and CO_2). The thermodynamic properties of the chemical species are evaluated using the nine-coefficient NASA polynomial representation (McBride, Zehe & Gordon 2002). The governing equations are discretized on Cartesian uniform grids and solved using the DCD (Dispersion Controlled Dissipation) scheme (Jiang 2004) with Strang's splitting. To overcome the stiffness problem, a sufficient number of sub-reaction steps are involved to ensure overall accuracy (Yee *et al.* 2013). To achieve sufficient numerical grid resolution for the simulations, standard MPI-based parallelization was implemented in the numerical code and the parallel mode of computation was executed on a 96 multi-core CPU high-performance computing facility. The numerical code has been used and validated in our previous studies to investigate different aspects of ODWs (Teng, Ng & Jiang 2017; Tian, Teng & Ng 2019).

The inflow is set to be a homogeneous stoichiometric hydrogen–air mixture with $H_2:O_2:N_2 = 2:1:3.76$ in all cases. The inflow conditions are fixed at the free-stream values along both the left and upper boundaries of the domain. The outflow conditions extrapolated from the interior under the assumption of zero first-order derivatives are implemented on the right and lower boundaries before the wedge. A slip boundary condition is used on the wedge surface, which starts from $x = 0$ on the lower computational boundary. Initially, the whole flow field has uniform density, velocity and pressure, which are calculated according to the inflow conditions and the wedge angle θ, fixed at $19°$. The simulations do not stop until the ODW flow field converges to a

steady state. Because of the multi-scale nature of the phenomena, both the computational domain and mesh scale are adjusted, and so resolution studies are conducted to ensure the global characteristic features are unaffected by the mesh properties. In all subsequent figures, the dimensions of temperature, pressure, density and heat release rate are K, Pa, kg m^{-3} and kJ cm^{-3} s^{-1}, respectively.

In most previous studies, the controlling parameters are those of the pre-detonation mixtures, such as velocity, temperature and pressure. To avoid artificial parametric variations and to cover a wide range of flight conditions, the controlling parameters are set to be the flight altitude H_0 and Mach number M_1. In the simulations, the parameters of the pre-detonation mixtures are first derived from H_0 and M_1, and then used as input variables in the codes. According to the standard atmosphere (King 1978), P_1 and T_1 can be determined by the flight altitude H_0, and the flow velocity V_1 can be obtained from M_1. Subsequently, the inflow is compressed twice by the OSW, whose parameters can be calculated through the Rankine–Hugoniot relations for the given oblique shock angle. The implicit relation between the oblique shock angle β_i ($i = 1, 2$) and the flow deflection angle φ_i ($i = 1, 2$) is given by

$$\tan^3 \beta_i + A \tan^2 \beta_i + B \tan \beta_i + C = 0, \tag{2.6}$$

where

$$\left. \begin{aligned} A &= \frac{1 - M_i^2}{\tan \varphi_i [1 + (\gamma - 1)M_i^2/2]}, \\ B &= \frac{1 + (\gamma + 1)M_i^2/2}{1 + (\gamma - 1)M_i^2/2}, \\ C &= \frac{1}{\tan \varphi_i [1 + (\gamma - 1)M_i^2/2]}. \end{aligned} \right\} \tag{2.7}$$

To satisfy the hypothesis for the inlet configuration of two equal-strength shocks, the normal Mach number in front of each oblique shock should be equal, that is,

$$M_1 \sin \beta_1 = M_2 \sin \beta_2. \tag{2.8}$$

By combining (2.6)–(2.8), the flow parameters after twice compressing, i.e. P_3, T_3 and V_3, can be deduced by the given fixed total flow deflection angle $\varphi = 24°$. These parameters are also taken as the inflow parameters before the ODW. Again, the mixing process is neglected, and thus a homogeneously premixed mixture enters the combustor.

3. Numerical results and discussion

3.1. *Effects of flight altitude and Mach number*

In this study, a total of 15 cases are simulated with different M_1 and H_0 values. Using the methods introduced above, the resulting pre-detonation parameters are calculated according to M_1 and H_0, as listed in table 1. Overall, there are three case groups. The first group includes cases 1 to 7, with a fixed $M_1 = 10.0$ and a variable H_0. The second group includes cases 8 to 11, with a variable M_1 and a fixed $H_0 = 30$ km. The third group, cases 12 to 15, also uses a variable M_1 but H_0 is fixed to be 20 km. The first case group is used to investigate the effects of H_0, while the other case groups are mainly for investigating the effects of M_1 with different altitudes. For the first case group, the pressure P_3 is sensitive to H_0, but the temperature T_3 and velocity V_3 are not: increasing H_0 decreases P_3 significantly, but there are only slight increases in T_3 and V_3.

Case no.	H_0 (km)	M_1	P_3 (kPa)	T_3 (K)	V_3 (m s^{-1})
Case 1	10	10.0	1202.9	958.1	2737.7
Case 2	15	10.0	549.8	929.8	2697.0
Case 3	20	10.0	251.0	929.8	2697.0
Case 4	25	10.0	115.7	950.8	2727.3
Case 5	30	10.0	54.3	972.1	2757.6
Case 6	35	10.0	26.1	1015.0	2817.9
Case 7	40	10.0	13.0	1074.4	2899.1
Case 8	30	9.5	48.2	910.3	2615.6
Case 9	30	9.0	42.5	851.5	2473.4
Case 10	30	8.5	37.3	795.7	2330.9
Case 11	30	8.0	32.5	742.8	2188.2
Case 12	20	10.5	281.7	991.9	2835.7
Case 13	20	9.5	222.5	870.6	2558.0
Case 14	20	9.0	196.3	814.4	2418.9
Case 15	20	8.5	172.2	761.0	2279.6

Table 1. Pressure, temperature and velocity of a stoichiometric hydrogen–air mixture at the combustor entrance of all presented cases.
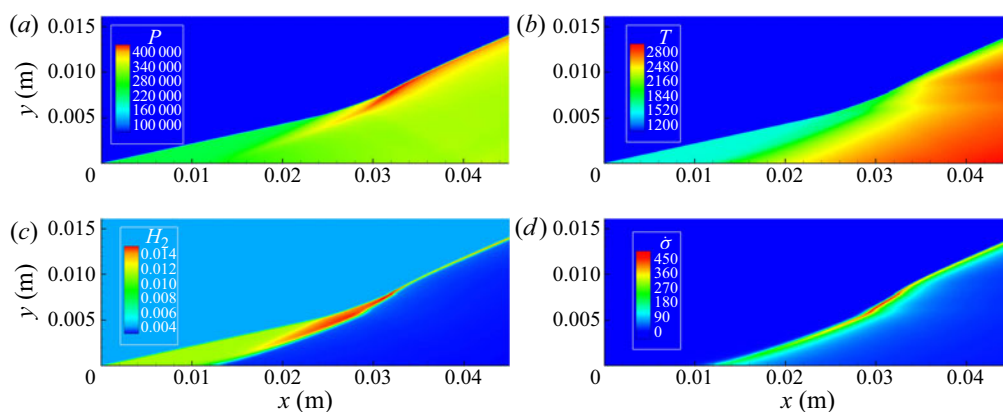

Figure 2. Pressure (*a*), temperature (*b*), H$_2$ density (*c*) and heat release rate (*d*) with $H_0 = 30$ km, $M_1 = 10.0$.

First of all, the ODW fields of case 5, with $H_0 = 30$ km and $M_1 = 10.0$, are displayed in figure 2 by pressure, temperature, H$_2$ density and heat release rate. The morphology indicates a simple structure: the OSW–ODW transition is smooth, and the ODW surface is stable with no fine structure. In the wave system of the initiation region, the pressure increase across the reactive front is trivial near the lower wedge, coupled with a modest temperature rise. When approaching the ODW surface, the pressure variation across the reactive front becomes obvious, coupled with a rapid temperature increase. Meanwhile, a post-shock region with high H$_2$ density can be observed, suggesting that there exists one CW in front of the heat release surface. This CW leads to the maximum heat release rate, as shown in figure 2(*d*). Despite different chemical reaction mechanisms, similar structures have been observed in previous studies (Teng & Jiang 2012; Yang *et al.* 2018, 2019*a*).
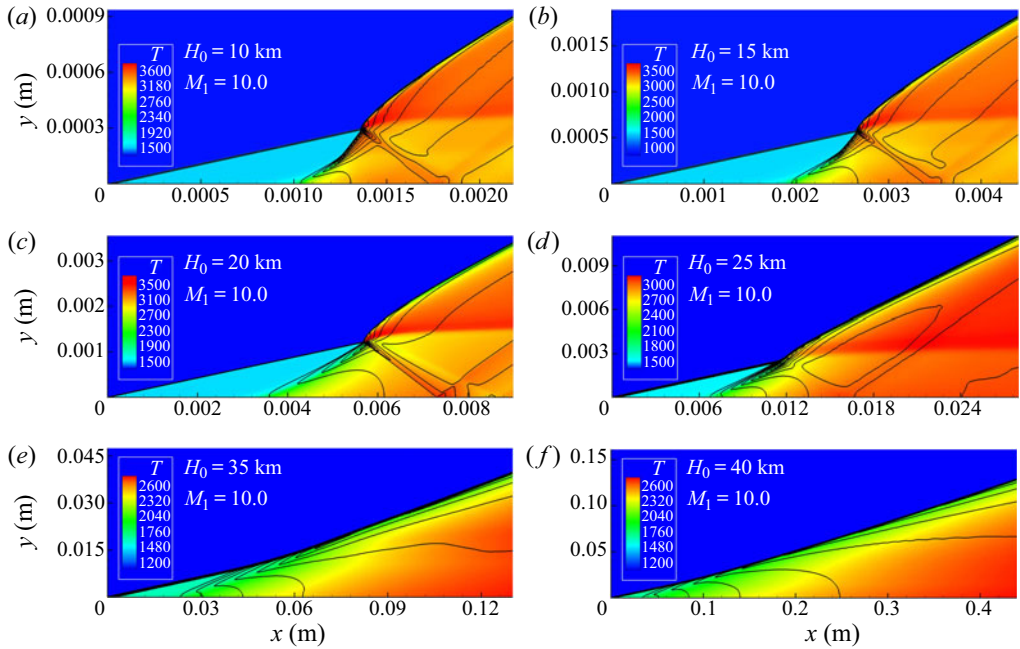
Figure 3. Temperature fields overlapped with pressure contours in the cases of $M_1 = 10.0$ and $H_0 = 10$ km (a), 15 km (b), 20 km (c), 25 km (d), 35 km (e), 40 km (f).

For the other cases of the first group, the temperature fields and pressure contours are displayed in figure 3. As one important aspect of the ODW morphology, the OSW–ODW transition varies with H_0: the transition is smooth for $H_0 = 35$ and 40 km and abrupt in the case of $H_0 = 10$, 15 and 20 km. In case 4 ($H_0 = 25$ km, shown in figure 3d), the transition is an intermediate type between the abrupt and smooth transitions. The different transition types can be attributed to variations in the inflow depending on H_0. As listed in appendix B, environmental gas temperature changes a little while pressure/density changes significantly when H_0 varies. For instance, the temperature rises from about 960 K in case 1 to about 1070 K in case 7, as shown in table 1. In contrast, the pressure decreases from about 1200 kPa to about 13 kPa, which has much greater variation than the temperature. From the equation of state, the density variation is close to the pressure variation, reflecting a dense inflow with low altitude and rare inflow with high altitude. Thus, the morphology is dominated by pressure or density, rather than by temperature. With a low H_0, the inflow becomes dense, so the angle difference between oblique shock and oblique detonation becomes large, as displayed in figure 3. The angle difference plays an important role in the OSW–ODW transition (Teng & Jiang 2012), i.e. a large difference induces an abrupt transition and vice versa. Hence, the transition type is abrupt with low H_0 and smooth with high H_0. On the contrary, a high temperature should induce a fast initiation of ODW with a high H_0, which does not occur due to the effects of the low pressure or density.

Regarding the wave system of the initiation region, CWs of different strengths arise from the wedge in all cases. When approaching the OSW–ODW surface, the pressure contours converge gradually to a narrow spatial region. Despite a stationary flow field, this wave distribution can be viewed as a convergence from the bottom up, named 'CW convergence'. For high values of H_0, the CW and its convergence are modest, as shown in figure 3(e,f). In contrast, the CW becomes strong with fast convergence in figure 3(a,b),
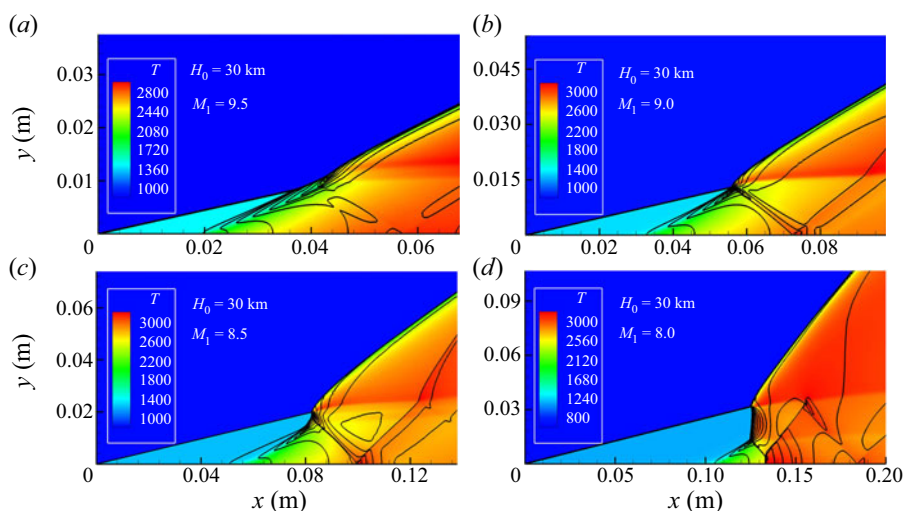
913 A1-8

Figure 4. Temperature fields overlapped with pressure contours in the cases of $H_0 = 30$ km and $M_1 = 9.5$ (*a*), 9.0 (*b*), 8.5 (*c*), 8.0 (*d*).

resulting in the oblique shock. This CW–OSW system also introduces another oblique shock and a slip line in the product, which are necessary to match the parameters of different zones. An intermediate wave system between the CW and CW–OSW may appear, such as that shown in figure 3(*c*,*d*).

To study the effects of changes in M_1, the ODWs of the second case group, with different values of M_1 and $H_0 = 30$ km, are shown in figure 4 by the temperature fields and pressure contours. As M_1 decreases from 10.0 to 9.5, the transition remains smooth and the wave system retains the CW, as shown in figure 4(*a*). Decreasing M_1 further to 9.0, however, causes the transition to change from smooth to abrupt, coupled with a strong CW overlapping on the reactive front, as shown in figure 4(*b*). Further decreasing M_1 to 8.5, one short Mach stem appears below the transition point, resulting in a more complicated wave system beneath the transition point in figure 4(*c*). In the case of $M_1 = 8.0$ (shown in figure 4*d*), the wave system features a long normal detonation wave (NDW) that covers over half of the length from the surface to the wedge. This long NDW coupled with the reactive front has not been observed in steady ODWs, although it has appeared in transient ODWs (Teng *et al.* 2014). The ODWs of the third group, with different values of M_1 and $H_0 = 20$ km, are shown in figure 5. This case group should be compared with that shown in figure 3(*c*), with an abrupt transition in the case of $M_1 = 10.0$. Increasing M_1 to 10.5 changes the transition to return smooth, and the CW arises clearly in figure 5(*a*). Decreasing M_1 leads to the abrupt transition, coupled with the CW–OSW wave system. From figure 5(*b*) to 5(*d*), the SODW becomes longer and the angle becomes larger, also leading to a long NDW. This trend of morphology variation is similar to that in figure 4, although a relatively high M_1 is necessary for generating similar structures. This is because the low H_0 corresponds to a dense inflow or high normalized heat release, so high M_1 is necessary for the standing of ODW to match the high Chapman–Jouguet (CJ) Mach number of the mixture inflow.

3.2. *Discussion of the two wave systems*

From the morphology observed in §3.1, some features of ODWs in a stoichiometric hydrogen–air mixture can be clarified. For the first aspect of the morphology, the
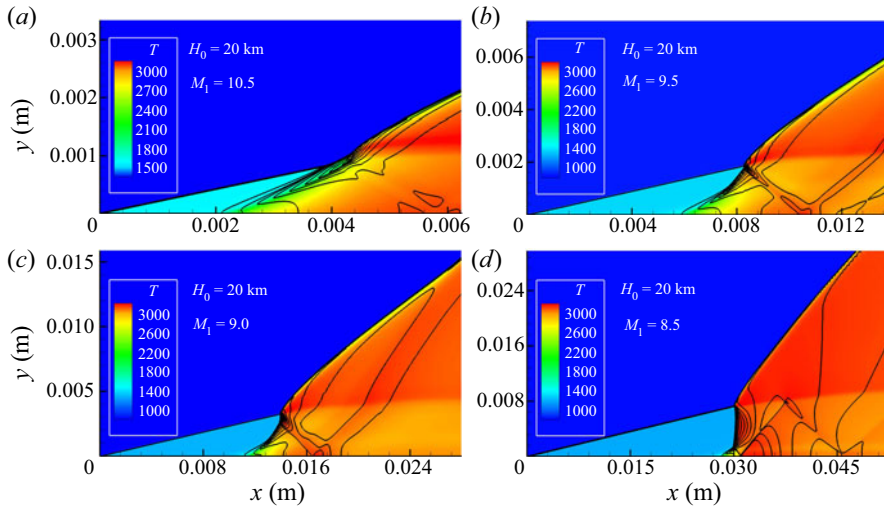
Figure 5. Temperature fields overlapped with pressure contours in the cases of $H_0 = 20$ km and $M_1 = 10.5$ (*a*), 9.5 (*b*), 9.0 (*c*), 8.5 (*d*).

OSW–ODW transition, both smooth and abrupt types appear. Their variation depends on H_0 and M_1, and can be predicted by previously reported criteria (Teng & Jiang 2012; Miao *et al.* 2018). For the second aspect, the ODW surface instability, all the surfaces are stable and free of fine structures. However, for the third aspect of the morphology, the wave system of the reactive front, several different wave configurations are observed. Among them, two wave systems deserve further detailed analysis, namely case 9 shown in figure 4(*b*) and case 11 shown in figure 4(*d*).

The ODW of case 9, displayed in figure 4(*b*), demonstrates a special wave system featuring a CW-induced abrupt transition. The CW usually appears in cases of smooth OSW–ODW transitions, whereas the SODW, which is actually a combination of an OSW and the reactive front, usually appears in cases of abrupt OSW–ODW transition. However, whether the CW could induce the abrupt transition, without the formation of either an OSW or SODW, has not been carefully studied. In case 9, the results reveal that the abrupt transition could appear together with the CW, leading to a morphology that has previously been ignored. To illustrate the characteristics of this morphology, pressure distributions along different lines parallel to the *x* axis for cases 9 and 10 are plotted in figure 6. As shown in figure 6(*a*), there is a gradual pressure increase along each curve, except for the final (pink) one. In contrast, a sharp pressure increase appears on curves 3–6 in figure 6(*b*), illustrating a shock rather than a CW. Note that the unavoidable diffusion means it is usually difficult to distinguish a shock from a strong CW when analysing the results from shock-capturing methods, although the former has a fixed number of mesh points while the latter does not when the simulation resolution changes. The rapid pressure increase, such as in curves 4 (black) and 5 (orange) in figure 6(*a*), might be thought of as a weak shock. However, if it is a shock, the coupling with heat release will result in a SODW in the shocked gas, whose peak pressure should be higher than that of the main ODW. This phenomenon is verified in figure 6(*b*), illustrating that the peak pressure behind the main ODW (curve 6) is less than that of curves 3–5. Nevertheless, in figure 6(*a*), the peak pressure is greatest on the pink curve, indicating, from another viewpoint, that there is only a CW.
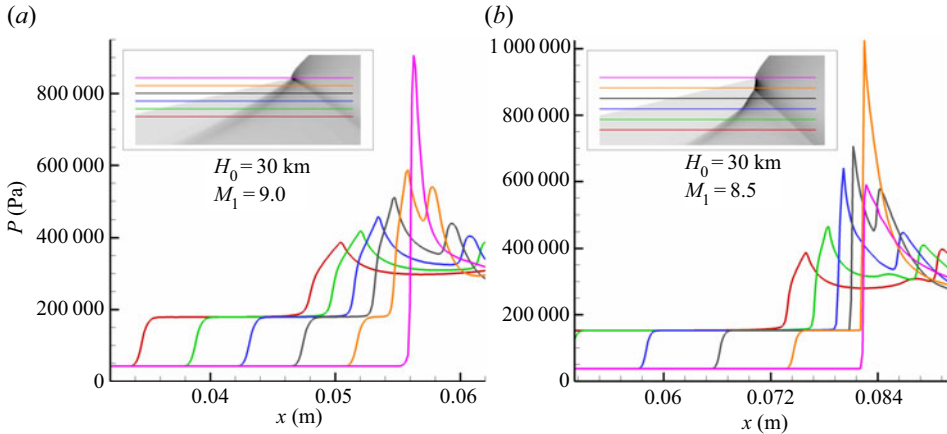
913 A1-10

Figure 6. Pressure along different lines parallel to the x axis in the cases of $H_0 = 30$ km, $M_1 = 9.0$ (*a*) and 8.5 (*b*).
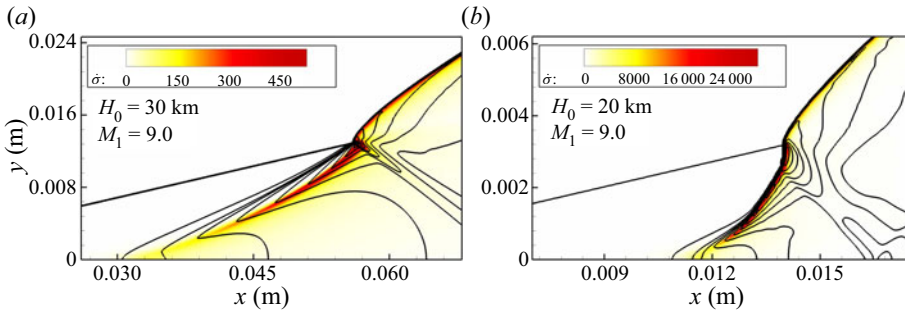

Figure 7. Heat release rate fields overlapped with pressure contours (black): (*a*) $H_0 = 30$ km, $M_1 = 9.0$; (*b*) $H_0 = 20$ km, $M_1 = 9.0$.

To analyse the CW-induced abrupt transition further, the heat release rate fields of cases 9 and 14, with the same $M_1 = 9.0$, are compared in figure 7. Overlapped with pressure contours, the CW evolution can be observed clearly. As shown in figure 7(*a*), the heat release induces the CW, indicated by the pressure contours in front of the main heat release layer. The pressure contours converge when they approach the surface, accelerating the heat release through a positive feedback. In case 14 shown in figure 7(*b*), the CW–OSW wave system appears, demonstrating a different wave configuration. Actually, this wave system is similar to that in figure 7(*a*) near the wedge, but the fast convergence of CW results in a SODW, which couples tightly with the heat release.

The coexistence of a CW and the abrupt transition helps understand the morphology in physical terms. Previously, the smooth and abrupt transitions were thought to correspond to the CW and OSW/SODW, respectively. The present morphological study demonstrates that, besides the smooth transition, the abrupt transition might be triggered by the CW, challenging the phenomenological connection of the transition type and the wave system. From the viewpoint of initiation, the CW or SODW may be viewed as the ignition source, and the smooth/abrupt transition viewed as the slow/fast initiation. Weak ignition by a CW usually induces the slow initiation, i.e. the smooth transition, and vice versa. However, given a strong enough CW, the fast initiation, i.e. the abrupt initiation, is
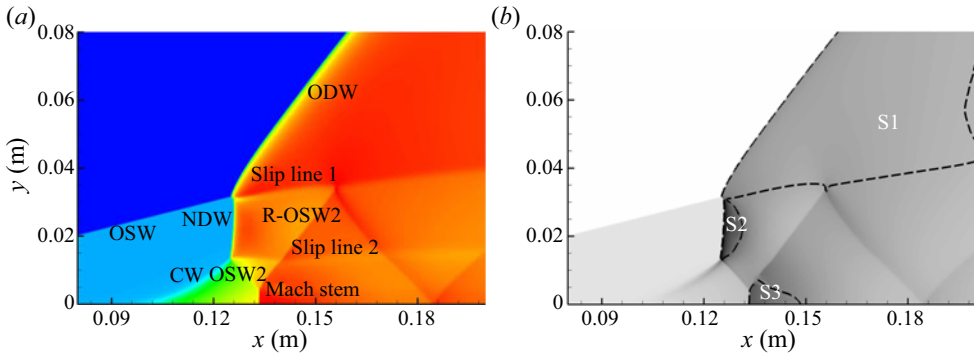
Figure 8. Temperature (*a*) and pressure with black sonic lines (*b*) in the case of $H_0 = 30$ km, $M_1 = 8.0$.

also possible. This is only a qualitative explanation, and further detailed quantitative analysis is necessary in the future.

It is worth noting that the ODW of case 11, displayed in figure 4(*d*), is another illustration of the well-known 'detonation-behind-shock' wave configurations observed elsewhere. Examples include initiation of high explosives in flyer plate experiments, the critical detonation diffraction problem where the transverse detonation sweeps through the unburnt materials behind the decoupled, diffracted shock and the final stage of the deflagration-to-detonation transition (Oppenheim, Laderman & Urtiew 1962; Arienti & Shepherd 2005; Khasainov *et al.* 2005; Menikoff & Shaw 2011). It is, however, noteworthy that the present wave configuration is also stationary. A similar flow field arises in case 15 (figure 5*d*), indicating it is a universal morphology. To investigate this special wave system, its local fields are shown in figure 8. On the reactive front, the lower part near the wedge is the CW, similar to the other cases. From the bottom up, the CW converges and ends with one NDW, rather than the usual SODW. In the product behind the reactive front, there is one oblique shock (OSW2) extending towards the wedge, and this induces a Mach stem and reflective OSW (R-OSW2). There are two slip lines observed in this wave system, originating from the two ends of the NDW. The near-field flow is subsonic behind the ODW (S1), the NDW (S2) and the Mach stem (S3), as shown in figure 8(*b*).

From the viewpoint of morphology, the formation of the NDW leads to a more complicated wave system. An upstream-facing NDW is thought to be impractical and should be avoided in an engine, attributed to the possible large total pressure loss. However, this NDW does not face the inflow directly, but locates behind the main OSW and normal to the pre-shocked gas rather than the inflow, so its effects on the propulsion performance should be examined in the future. For a long time, whether it was possible to have a NDW in the initiation region was not addressed in ODW research. Our recent study (Zhang *et al.* 2019) has demonstrated the possibility of a NDW in this region, but the spatiotemporal scale is too short for detailed analysis. A similar short stem also appears in case 10, as displayed in figure 6(*b*). This wave system is composed of three sections, namely a lower CW, middle SODW and upper NDW. In case 11, the CW does not converge to become an OSW or SODW, but instead to become a normal shock or NDW. These structural variations indicate that there are underlying connections among the various wave systems, suggesting a study of the wave system by analysing the flow characteristics, rather than building the phenomenological connection.
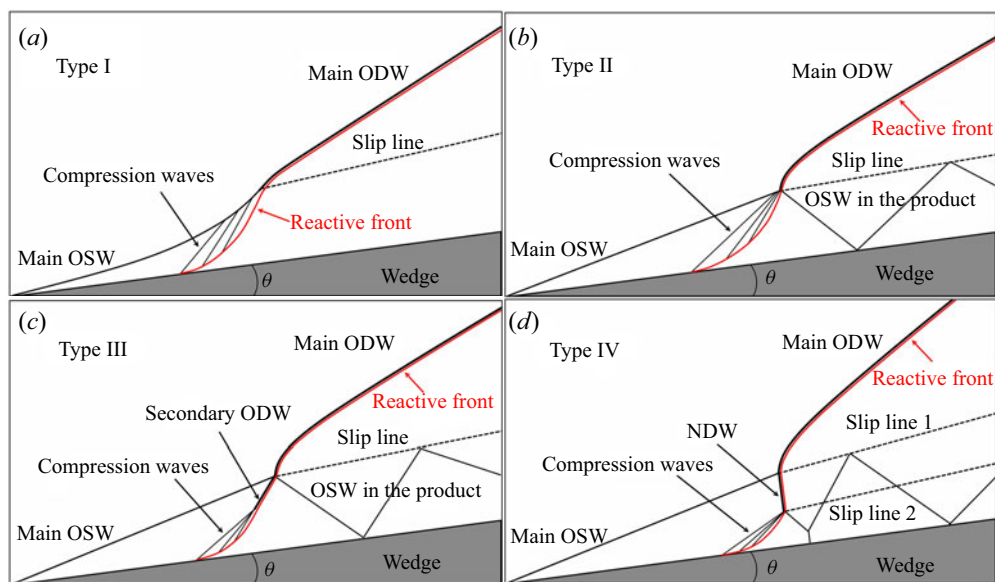
913 A1-12

Figure 9. Morphology of ODWs with different wave systems.

3.3. *Analysis of the flow characteristics*

Using the control parameters of flight altitude H_0 and Mach number M_1, the morphological variation becomes clearer, which might be helpful in engineering applications. Both H_0 and M_1 influence the morphology, although there is greater sensitivity to M_1 than to H_0. In the parametric range considered in this study, $H_0 = 10$–40 km and $M_1 = 8.0$–10.0, the smooth transition with simple wave systems appears with high H_0 and M_1, and the abrupt transition with complicated wave systems appears with low H_0 and M_1. Moreover, decreasing H_0 and M_1 may change the morphology, leading to the SODW or the NDW.

The morphology of ODWs has been studied by many researchers, but there are still some structural ambiguities. According to the wave systems presented above, the latest knowledge on the morphology is illustrated in figure 9. There are four different wave systems, named Type I–IV. The first morphology type features the smooth transition and the CW system, which was identified in early research. The CW is generated by the heat release and interacts with the main OSW, which is deflected gradually. Figure 9(b) features the abrupt transition and the CW system, the existence of which was described in the previous subsection. In figure 9(c), the abrupt transition appears with the SODW system, a configuration that has been known for some time (Ghorbanian & Sterling 1996). However, prior studies have not determined the existence of the CW near the wedge. By revisiting studies claiming the existence of this SODW, such as Liu *et al.* (2016), the CW can be observed despite its brief appearance, suggesting that the CW is unavoidable. For the fourth morphology type in figure 9(d), the CW converges rapidly, leading to the special wave system composed of a CW–NDW complex. Note that the morphology transition depends on M_1 and H_0 continuously, so certain ODWs might be hard to classify into one type. To elucidate the morphology transition beyond phenomenological connections, it is necessary to analyse the wave system from the viewpoint of the wave evolution, especially the CW behaviour which is unavoidable in all the wave systems.

The origin of the CW is attributable to heat release in the shocked flow. To clarify the physical law, figure 10(a) demonstrates the variations of heat release rate along the
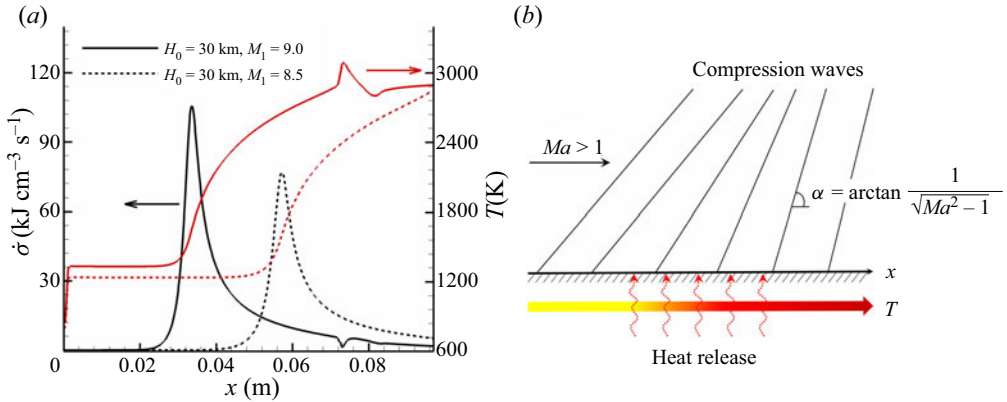
Figure 10. (*a*) Heat release rate and temperature along the streamlines of $y = 0$ m in cases 9 and 10. (*b*) Schematic of Mach lines of supersonic flow with heat addition.

lines of $y = 0$ m in cases 9 and 10. It can be observed that the heat release increases first and decreases subsequently, leading to a high temperature downstream. According to the gas-dynamic theory (Liepmann & Roshko 2001), the heat addition of supersonic flow leads to the decrease of local Mach number. Therefore, the Mach lines derived from the streamline of $y = 0$ m will converge, because the angles upstream are small while the angles downstream are large, as shown in figure 10(*b*). Similar processes occur along other x axis parallel streamlines, and cumulative effects should be considered when the CW approaches the OSW–ODW surface. Therefore, the CW convergence along the reactive front is the critical process determining the wave system.

To elucidate the CW-related wave system, a theoretical study based on geometric analysis through double Mach lines has been conducted. This theoretical method depends on two key parameters, H_{CW} and H_{ini}. The former is the height of the CW, above which the CW may be replaced by the SODW or NDW, so it effectively quantifies the CW convergence. The latter is the height of the initiation region, i.e. the distance between the wedge and the transition point of the OSW–ODW surface. If H_{CW} is less than H_{ini}, the CW will converge to the shock, resulting in either a SODW or NDW; otherwise, there is only one CW in the wave system. Considering that H_{ini} is available from the numerical results, the critical step is to determine H_{CW}. For simplicity, H_{CW} is calculated from the double Mach lines, as illustrated in figure 11. The CW front is denoted by the first blue Mach line, starting from the x axis at the point where the heat release rate reaches 50 % of its peak value along the near-wedge streamline. The CW tail is denoted by the second red Mach line, starting from the x axis at the point where the maximum heat release rate is achieved. In the future, more elaborate methods could be employed to consider several curved Mach lines. The inclination angle of the Mach line is calculated by the local flow Mach number as shown in figure 10(*b*), resulting in an intersection point at a distance from the wedge of H_{CW}. Figure 11(*a*) illustrates that H_{CW} is less than H_{ini} in case 10, indicating that the CW converges quickly enough to generate a shock wave coupled with the reactive front, i.e. the formation of a SODW. On the contrary, H_{CW} is larger than H_{ini} in figure 11(*b*), so there is only a CW in case 5. Note that the intersection of two Mach lines is unavoidable, being determined by the feature of supersonic flow with energy input. Thus, the determination of double Mach lines offers an effectively quantitative evaluation criterion for the detailed physical mechanism.
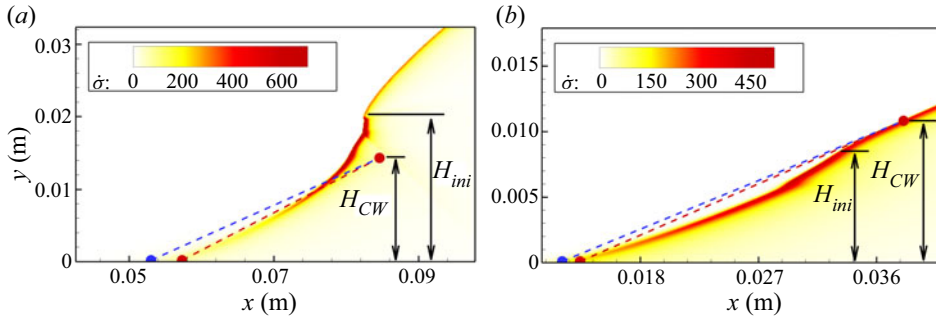
913 A1-14

Figure 11. Enlarged initiation zone in the cases of (*a*) $M_1 = 8.5$, $H_0 = 30$ km and (*b*) $M_1 = 10.0$, $H_0 = 30$ km.

Case no.	H_{ini} (mm)	H_{CW} (mm)	H_{ini}/H_{CW}	Type
Case 1	0.29	0.15	2.00	III
Case 2	0.58	0.36	1.59	III
Case 3	1.22	1.08	1.12	II
Case 4	2.72	3.04	0.90	I
Case 5	8.45	10.83	0.78	I
Case 6	16.57	37.09	0.45	I
Case 7	48.55	117.70	0.41	I
Case 8	11.45	11.80	0.97	I
Case 9	12.90	12.41	1.04	II
Case 10	19.84	14.36	1.38	III
Case 11	31.51	15.47	2.04	IV
Case 12	0.96	0.96	0.99	I
Case 13	1.87	1.10	1.71	III
Case 14	3.23	1.16	2.78	III
Case 15	7.26	1.38	5.26	IV

Table 2. Geometric parameters determined by the near-wedge streamlines in all cases.

Results of geometric analysis for all the cases are listed in table 2, with the corresponding morphology type sketched in figure 9. Obviously, H_{CW} increases when M_1 remains at 10.0 and H_0 increases (cases 1–7). For the other two case groups, i.e. cases 8–11 and cases 12–15, H_{CW} also increases when M_1 decreases and H_0 remains at 30 or 20 km. On the other hand, H_{ini} follows the same trend as H_{CW}, but more modestly. Thus, the ratio of H_{ini}/H_{CW} becomes smaller as H_0 increases, and larger as M_1 decreases. For cases 1–7, the ratio decreases and the morphology type changes from III to I, that is, from SODW to CW-induced smooth ODW. For the other groups, the ratio increases and the morphology type changes from I to IV, correspondingly. When the ratio H_{ini}/H_{CW} is greater than about 1.2, the CW convergence induces the shock wave, resulting in either SODW or NDW. The deviation of H_{ini}/H_{CW} from unity can be attributed to the simplification of the double Mach lines, which are supposed to be straight. However, these results indicate that the model of CW convergence can be used to predict the wave system with limited error, providing new insights into the morphology of ODWs. The ratio values in table 2 may be different if we chose other ways to define H_{CW}, but the variation trend and their association with the morphology type should be the same.

A previous study (Teng *et al.* 2017) has approximated the initial heat release along the near-wedge streamline as a constant volume explosion process, leading to a theoretical model to estimate the ODW initiation length. Inspired by that work, we develop a method considering the detailed interaction of flow and heat release along the near-wedge streamline to determine H_{CW} theoretically. Given mixture parameters P_3, T_3, V_3 and wedge angle θ, (2.6) and (2.7) could be used to calculate the gas parameters compressed by the main OSW. Then, an integration of the following equations (Kao & Shepherd 2008) is performed from the post-shock state and the beginning of the wedge surface:

$$\frac{\mathrm{d}\rho}{\mathrm{d}x} = -\frac{\rho\dot{\tilde{\sigma}}}{V(1 - Ma^2)}, \tag{3.1}$$

$$\frac{\mathrm{d}V}{\mathrm{d}x} = \frac{\dot{\tilde{\sigma}}}{1 - Ma^2}, \tag{3.2}$$

$$\frac{\mathrm{d}P}{\mathrm{d}x} = -\frac{\rho V \dot{\tilde{\sigma}}}{1 - Ma^2}, \tag{3.3}$$

$$\frac{\mathrm{d}Y_i}{\mathrm{d}x} = -\frac{\dot{\omega}_i}{\rho V}. \tag{3.4}$$

The normalized heat release rate $\dot{\tilde{\sigma}}$ is calculated by

$$\dot{\tilde{\sigma}} = \sum_{i=1}^{n} \left(\frac{\bar{w}}{w_i} - \frac{h_i}{c_p T} \right) \frac{\mathrm{d}Y_i}{\mathrm{d}t}, \tag{3.5}$$

where $\bar{w}$ is mean molecular weight of the mixture, c_p is the mixture frozen specific heat and Y_i is species' mass fraction. These calculations follow the methods of calculating Zel'dovich–von Neumann–Döring structures of one-dimensional steady detonations, leading to a heat release curve like the one in figure 10(*a*). Thereafter, theoretical H_{CW} could be calculated following the same procedure discussed above, and the results are shown in figure 12. Generally speaking, the theoretical H_{ini}/H_{CW} values are higher than the corresponding numerical ones, by about 1.5 times. The decreasing from cases 1 to 7 and increasing of the other two case groups are obvious, which shows the same variation trends as those of the numerical results. These results indicate that an analytical H_{CW} is applicable for predicting the morphology type, although the detailed values are different from those based on numerical results.

The theoretical study based on H_{CW} and H_{ini} explains the mechanism of shock formation induced by a CW in the initiation region, but the formation of SODW (Type III) or NDW (Type IV) requires further clarification. By examining the velocity parameters, we find that the Mach number ratio M_S/M_{CJ} provides a good prediction of the wave system difference (see table 3). Here M_S denotes the local Mach number of post-OSW mixtures, whereas M_{CJ} denotes the CJ Mach number of post-OSW mixtures. The parameters remain almost constant in the initial region of the post-OSW mixture along the near-wedge streamline, facilitating the determination of M_S and M_{CJ}. In particular, M_{CJ} is calculated based on the mass fractions of all species along with the pressure and temperature. The results in table 3 indicate that M_S changes little from cases 1 to 7, whereas M_{CJ} decreases slightly, so M_S/M_{CJ} increases. From cases 8 to 11, or cases 12 to 15, M_S decreases monotonically while M_{CJ} increases, which leads to a decrease in M_S/M_{CJ}. In general, the ratio of M_S/M_{CJ} decreases as H_0 and M_1 decrease, and the wave system changes to become Type IV when the ratio drops close to unity. This indicates that M_S/M_{CJ} can be accurately used
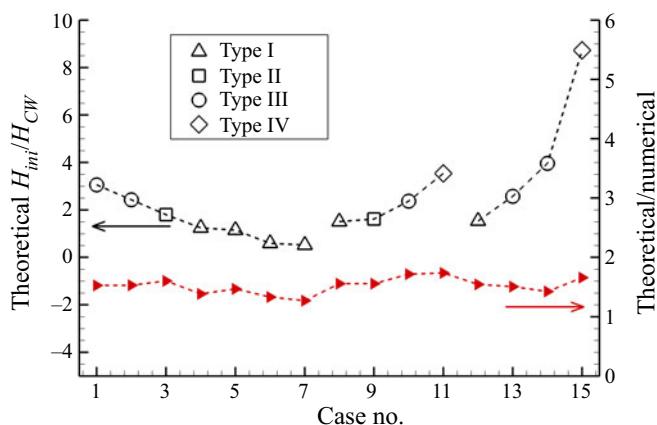
Figure 12. Theoretical results of H_{ini}/H_{CW} and corresponding wave systems for all cases.

Case no.	M_S	M_{CJ}	M_S/M_{CJ}
Case 1	2.678	2.221	1.206
Case 2	2.673	2.222	1.203
Case 3	2.699	2.183	1.237
Case 4	2.676	2.129	1.257
Case 5	2.681	2.068	1.296
Case 6	2.687	1.984	1.354
Case 7	2.697	1.886	1.430
Case 8	2.623	2.148	1.221
Case 9	2.559	2.232	1.147
Case 10	2.491	2.320	1.074
Case 11	2.414	2.412	1.001
Case 12	2.727	2.113	1.290
Case 13	2.615	2.269	1.153
Case 14	2.551	2.353	1.084
Case 15	2.481	2.442	1.016

Table 3. Velocity parameters of post-shock mixture in all cases.

to distinguish the formation of NDW, although the ratio does not perform as well as the first method in terms of the classification of wave systems.

These two analysis results enable us to achieve a further understanding of the morphology of ODWs, especially the complicated wave systems in the initiation region. In essence, these two methods attempt to quantify the key mechanisms in the sophisticated flow concerning the coupling of shock wave, expansion wave and heat release. The former method provides a wave evolution viewpoint, revealing the critical factor of the wave system and the OSW–ODW transition type. The latter analysis of the induction zone Mach number provides an overall assessment, i.e. slow post-OSW flow and large-scale heat release promoting CW convergence, and demonstrates that the NDW may appear when the Mach number ratio M_S/M_{CJ} is close to unity. This result also suggests that the stationary wedge-induced ODW may be associated with M_S, probably leading to the detached ODW when M_S/M_{CJ} is less than unity. Both methods have their merits and limitations, but a theoretical approach regarding the morphology of ODWs has been

collectively established. These results also suggest that ODWs are too complicated to be described by semi-empirical methods, and so future work should focus on mechanisms beyond phenomenological connections. Moreover, although the present work has used the reactive Euler equations to simplify the problem, future study should take into consideration more non-perfect fluid phenomena such as boundary layers, fuel injection and mixing, turbulence and encompassed deflagration waves and pockets, which would better address the ODW phenomenon in reality.

4. Conclusions

The ODW morphology has been studied numerically and theoretically. Previously, wave systems were usually considered empirically as SODWs or CWs, introducing some structural ambiguities. This study simulated the ODWs in a stoichiometric hydrogen–air mixture first, with the controlling parameters H_0 and M_1. Two wave systems were then analysed and discussed, one indicating that the CW may also induce the abrupt transition and the other suggesting that the classical SODW may evolve into a NDW. Hence, four ODWs with different wave systems were sketched and their relations were discussed based on these phenomena. To clarify the mechanisms of the different wave systems, a semi-theoretical study of the morphology of ODWs has been conducted by two analysis approaches. One relies on geometric analysis through double Mach lines, revealing that the wave system could be predicted from the viewpoint of CW convergence. The other analyses the induction zone flow Mach number in comparison with the corresponding CJ Mach number, providing a criterion for NDW formation.

Declaration of interests. The authors report no conflict of interest.

Author ORCIDs.

Ⓓ Honghui Teng https://orcid.org/0000-0003-0943-4553;

Ⓓ Lin Zhou https://orcid.org/0000-0003-3900-1345;

Ⓓ Hoi Dick Ng https://orcid.org/0000-0002-8459-5990.

Appendix A

The numerical detonation simulation results are sensitive to the grid length scale. In this paper, the numerical grid resolution used for different cases varies from a coarse mesh of 400 µm to a fine mesh of 4 µm. To ensure the independence of the results with respect to the grid scale, a resolution study is performed by doubling the grid numbers in both the x and y directions at the same time. For instance, the density contours of case 9 with the default mesh size of 400 µm are shown in figure 13, and compared with the results with the refined mesh size of 200 µm. It can be seen that the differences between the two wave structures are difficult to distinguish. A quantitative comparison is conducted by plotting the pressure and temperature along three typical lines (i.e. $y = 0$ m, 0.02 m and 0.08 m), as shown in figure 14. These lines correspond to different flow regions of the ODW field, including the wedge surface, NDW structures and steady ODW surface. The curves nearly overlap with trivial differences, so a grid of 400 µm is sufficient to capture the main ODW structures of case 9. Another example examining the effect of mesh size in case 5 is shown by the density contours in figure 15 and the quantitative comparison in figure 16. Again, the two wave structures are similar to each other, though a
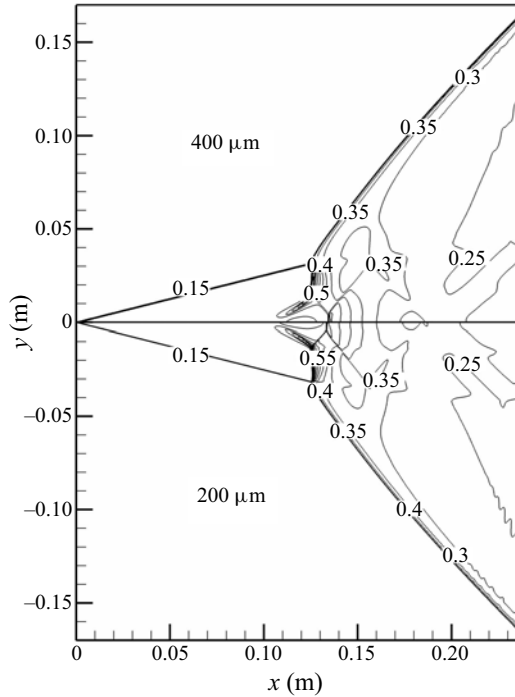
Figure 13. Density fields with different grid scales in the case of $H_0 = 30$ km, $M_1 = 8.0$.
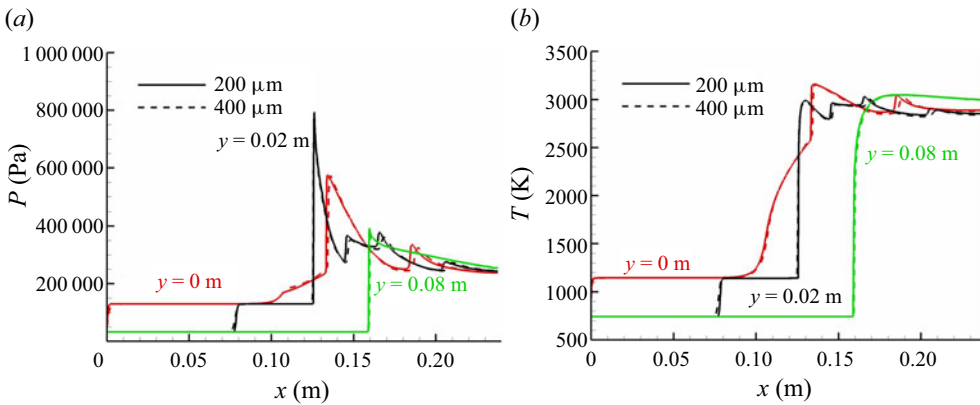

Figure 14. (*a*) Pressure and (*b*) temperature along different lines parallel to the x axis with different grid scales in the case of $H_0 = 30$ km, $M_1 = 8.0$.

slight quantitative discrepancy appears near the oblique detonation surface. For other cases with different M_1 and H_0, similar resolution studies have been performed to eliminate the effects of grid size. Considering the main issues discussed in this work, the chosen grid scale provides converged, global formation structures that are sufficient to guarantee the reliability of the conclusions.
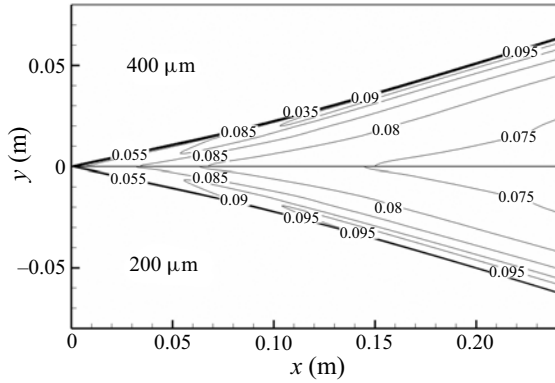
Figure 15. Density fields with different grid scales in the case of $H_0 = 40$ km, $M_1 = 10.0$.
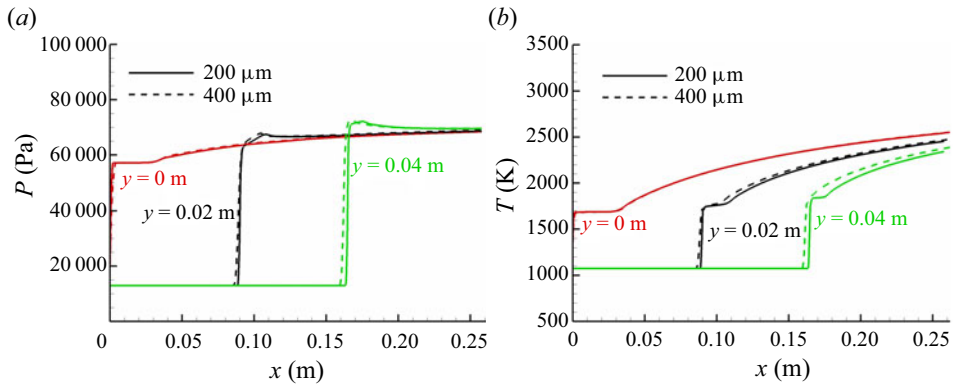

Figure 16. (*a*) Pressure and (*b*) temperature along different lines parallel to the x axis with different grid scales in the case of $H_0 = 40$ km, $M_1 = 10.0$.

Case no.	P_1 (kPa)	T_1 (K)	ρ_1 (kg m^{-3})	φ_1 (deg.)	β_1 (deg.)	φ_2 (deg.)	β_2 (deg.)
Case 1	26.50	223.3	0.414	9.67	14.08	14.33	21.09
Case 2	12.11	216.7	0.195	9.67	14.08	14.33	21.09
Case 3	5.53	216.7	0.089	9.67	14.08	14.33	21.09
Case 4	2.55	221.6	0.040	9.67	14.08	14.33	21.09
Case 5	1.20	226.5	0.018	9.67	14.08	14.33	21.09
Case 6	0.57	236.5	0.008	9.67	14.08	14.33	21.09
Case 7	0.29	250.3	0.004	9.67	14.08	14.33	21.09
Case 8	1.20	226.5	0.018	9.76	14.40	14.24	21.24
Case 9	1.20	226.5	0.018	9.86	14.75	14.14	21.42
Case 10	1.20	226.5	0.018	9.95	15.14	14.05	21.64
Case 11	1.20	226.5	0.018	10.04	15.57	13.96	21.91
Case 12	5.53	216.7	0.089	9.58	13.79	14.42	20.97
Case 13	5.53	216.7	0.089	9.76	14.40	14.24	21.24
Case 14	5.53	216.7	0.089	9.86	14.75	14.14	21.42
Case 15	5.53	216.7	0.089	9.95	15.14	14.05	21.64

Table 4. Inflow gas-dynamic parameters and inlet compression angles of all presented cases.

Appendix B

Environmental gas pressure, temperature and density for each case are listed in table 4, corresponding to the parameters at state 1 in figure 1. Furthermore, the two flow deflection angles of inlet compression used in the simulations are also listed, which could lead to two equal-strength OSWs.

REFERENCES

ALEXANDER, D.C., SISLIAN, J.P. & PARENT, B. 2006 Hypervelocity fuel/air mixing in mixed-compression inlets of shcramjets. *AIAA J.* **44**, 2145–2155.

ARIENTI, M. & SHEPHERD, J.E. 2005 A numerical study of detonation diffraction. *J. Fluid Mech.* **529**, 117–146.

BDZIL, J.B., SHORT, M. & CHIQUETE, C. 2020 Transients following the loss of detonation confinement. *J. Fluid Mech.* **886**, A27.

BURKE, M.P., CHAOS, M., JU, Y., DRYER, F.L. & KLIPPENSTEIN, S.J. 2012 Comprehensive H_2/O_2 kinetic model for high-pressure combustion. *Intl J. Chem. Kinet.* **44**, 444–474.

CAMBIER, J.L., ADELMAN, H.G. & MENEES, G. 1990 Numerical simulations of an oblique detonation wave engine. *J. Propul. Power* **6**, 315–323.

CHOI, J.Y., KIM, D.W., JEUNG, I.S., MA, F. & YANG, V. 2007 Cell-like structure of unstable oblique detonation wave from high-resolution numerical simulation. *Proc. Combust. Inst.* **31**, 2473–2480.

CHOI, J.Y., SHIN, E.J.R. & JEUNG, I.S. 2009 Unstable combustion induced by oblique shock waves at the non-attaching condition of the oblique detonation wave. *Proc. Combust. Inst.* **32**, 2387–2396.

DUDEBOUT, R., SISLIAN, J.P. & OPPITZ, R. 1998 Numerical simulation of hypersonic shock-induced combustion ramjets. *J. Propul. Power* **14**, 869–879.

FANG, Y., ZHANG, Y., DENG, X. & TENG, H. 2019*a* Structure of wedge-induced oblique detonation in acetylene-oxygen-argon mixtures. *Phys. Fluids* **31**, 026108.

FANG, Y., ZHANG, Z. & HU, Z. 2019*b* Effects of boundary layer on wedge-induced oblique detonation structures in hydrogen-air mixtures. *Intl J. Hydrogen Energ.* **44**, 23429–23435.

FIGUEIRA DA SILVA, L.F. & DESHAIES, B. 2000 Stabilization of an oblique detonation wave by a wedge: a parametric numerical study. *Combust. Flame* **121**, 152–166.

GHORBANIAN, K. & STERLING, J.D. 1996 Influence of formation processes on oblique detonation wave stabilization. *J. Propul. Power* **12**, 509–517.

IWATA, K., NAKAYA, S. & TSUE, M. 2017 Wedge-stabilized oblique detonation in an inhomogeneous hydrogen-air mixture. *Proc. Combust. Inst.* **36**, 2761–2769.

JIANG, Z. 2004 On dispersion-controlled principles for non-oscillatory shock-capturing schemes. *Acta Mechanica Sin.* **20**, 1–15.

KAO, S. & SHEPHERD, J.E. 2008 Numerical solution methods for control volume explosions and ZND detonation structure. *Tech. Rep.* GALCIT Report FM2006.007. California Institute of Technology, Pasadena, California.

KHASAINOV, B., PRESLES, H.N., DESBORDES, D., DEMONTIS, P. & VIDAL, P. 2005 Detonation diffraction from circular tubes to cones. *Shock Waves* **14**, 187–192.

KING, R.L. 1978 A computer version of the U.S. Standard Atmosphere, 1976. *Tech. Rep.* NASA-CR-150778. Science Applications, Inc.

LAGUARDA, L., HICKEL, S., SCHRIJER, F.F.J. & VAN OUDHEUSDEN, B.W. 2020 Dynamics of unsteady asymmetric shock interactions. *J. Fluid Mech.* **888**, A18.

LI, C., KAILASANATH, K. & ORAN, E.S. 1993 Effects of boundary layers on oblique-detonation structures. *AIAA Paper* 1993-0450.

LI, C., KAILASANATH, K. & ORAN, E.S. 1994 Detonation structures behind oblique shocks. *Phys. Fluids* **6**, 1600–1611.

LI, G., ZHANG, G., ZHANG, Y., JI, L. & GAO, S. 2020 Influence of viscous boundary layer on initiation zone structure of two-dimensional oblique detonation wave. *Aerosp. Sci. Technol.* **104**, 106019.

LIEPMANN, H.W. & ROSHKO, A. 2001 *Elements of Gas Dynamics*. Dover Publications.

LIU, Y., LIU, Y.S., WU, D. & WANG, J.P. 2016 Structure of an oblique detonation wave induced by a wedge. *Shock Waves* **26**, 161–168.

LIU, Y., WU, D., YAO, S. & WANG, J.P. 2015 Analytical and numerical investigations of wedge-induced oblique detonation waves at low inflow Mach number. *Combust. Sci. Technol.* **187**, 843–856.

MCBRIDE, B.J., ZEHE, M.J. & GORDON, S. 2002 NASA Glenn coefficients for calculating thermodynamic properties of individual species. *Tech. Rep.* NASA/TP-2002-211556. NASA Glenn Research Center, Cleveland.

MENEES, G.P., ADELMAN, H.G. & CAMBIER, J.L. 1991 Analytical and experimental investigations of the oblique detonation wave engine concept. *Tech. Rep.* NASA-TM-102839. NASA Ames Research Center, Moffett Field, California.

MENIKOFF, R. & SHAW, M.S. 2011 Modeling detonation waves in nitromethane. *Combust. Flame* **158**, 2549–2558.

MIAO, S., ZHOU, J., LIU, S. & CAI, X. 2018 Formation mechanisms and characteristics of transition patterns in oblique detonations. *Acta Astronaut.* **142**, 121–129.

OPPENHEIM, A.K., LADERMAN, A.J. & URTIEW, P.A. 1962 The onset of retonation. *Combust. Flame* **6**, 193–197.

POWERS, J.M. & STEWART, D.S. 1992 Approximate solutions for oblique detonations in the hypersonic limit. *AIAA J.* **30**, 726–736.

PRATT, D.T., HUMPHREY, J.W. & GLENN, D.E. 1991 Morphology of standing oblique detonation waves. *J. Propul. Power* **7**, 837–845.

RADULESCU, M.I. 2018 A detonation paradox: why inviscid detonation simulations predict the incorrect trend for the role of instability in gaseous cellular detonations? *Combust. Flame* **195**, 151–162.

REN, Z., WANG, B., XIANG, G., ZHAO, D. & ZHENG, L. 2019*a* Supersonic spray combustion subject to scramjets: progress and challenges. *Prog. Aerosp. Sci.* **105**, 40–59.

REN, Z., WANG, B., XIANG, G. & ZHENG, L. 2018 Effects of the multiphase composition in a premixed fuel-air stream on wedge-induced oblique detonation stabilization. *J. Fluid Mech.* **846**, 411–427.

REN, Z., WANG, B., XIANG, G. & ZHENG, L. 2019*b* Numerical analysis of wedge-induced oblique detonations in two-phase kerosene-air mixtures. *Proc. Combust. Inst.* **37**, 3627–3635.

SHORT, M. & QUIRK, J.J. 2018 High explosive detonation-confiner interactions. *Annu. Rev. Fluid Mech.* **50**, 215–242.

SISLIAN, J.P., SCHIRMER, H., DUDEBOUT, R. & SCHUMACHER, J. 2001 Propulsive performance of hypersonic oblique detonation wave and shock-induced combustion ramjets. *J. Propul. Power* **17**, 599–604.

TENG, H., NG, H.D. & JIANG, Z. 2017 Initiation characteristics of wedge-induced oblique detonation waves in a stoichiometric hydrogen-air mixture. *Proc. Combust. Inst.* **36**, 2735–2742.

TENG, H., NG, H.D., LI, K., LUO, C. & JIANG, Z. 2015 Evolution of cellular structures on oblique detonation surfaces. *Combust. Flame* **162**, 470–477.

TENG, H.H. & JIANG, Z.L. 2012 On the transition pattern of the oblique detonation structure. *J. Fluid Mech.* **713**, 659–669.

TENG, H.H., JIANG, Z.L. & NG, H.D. 2014 Numerical study on unstable surfaces of oblique detonations. *J. Fluid Mech.* **744**, 111–128.

TIAN, C., TENG, H.H. & NG, H.D. 2019 Numerical investigation of oblique detonation structure in hydrogen-oxygen mixtures with Ar dilution. *Fuel* **252**, 496–503.

VALORANI, M., DI GIACINTO, M. & BUONGIORNO, C. 2001 Performance prediction for oblique detonation wave engines (ODWE). *Acta Astronaut.* **48**, 211–228.

VERREAULT, J., HIGGINS, A.J. & STOWE, R.A. 2013 Formation of transverse waves in oblique detonations. *Proc. Combust. Inst.* **34**, 1913–1920.

VIGUIER, C., GOURARA, A. & DESBORDES, D. 1996 Onset of oblique detonation waves: comparison between experimental and numerical results for hydrogen-air mixture. *Symp. (Intl) Combust.* **26**, 3023–3031.

WANG, K., TENG, H., YANG, P. & NG, H.D. 2020 Numerical investigation of flow structures resulting from the interaction between an oblique detonation wave and an upper expansion corner. *J. Fluid Mech.* **903**, A28.

WANG, T., ZHANG, Y., TENG, H., JIANG, Z. & NG, H.D. 2015 Numerical study of oblique detonation wave initiation in a stoichiometric hydrogen-air mixture. *Phys. Fluids* **27**, 096101.

WOLAŃSKI, P. 2013 Detonative propulsion. *Proc. Combust. Inst.* **34**, 125–158.

YANG, P., NG, H.D. & TENG, H. 2019*a* Numerical study of wedge-induced oblique detonations in unsteady flow. *J. Fluid Mech.* **876**, 264–287.

YANG, P., TENG, H., JIANG, Z. & NG, H.D. 2018 Effects of inflow mach number on oblique detonation initiation with a two-step induction-reaction kinetic model. *Combust. Flame* **193**, 246–256.

YANG, P., TENG, H., NG, H.D. & JIANG, Z. 2019*b* A numerical study on the instability of oblique detonation waves with a two-step induction-reaction kinetic model. *Proc. Combust. Inst.* **37**, 3537–3544.

913 A1-22

YEE, H.C., KOTOV, D.V., WANG, W. & SHU, C.W. 2013 Spurious behavior of shock-capturing methods by the fractional step approach: problems containing stiff source terms and discontinuities. *J. Comput. Phys.* **241**, 266–291.

ZHANG, Y., FANG, Y., NG, H.D. & TENG, H. 2019 Numerical investigation on the initiation of oblique detonation waves in stoichiometric acetylene-oxygen mixtures with high argon dilution. *Combust. Flame* **204**, 391–396.

ZHANG, Y., ZHOU, L., GONG, J., NG, H.D. & TENG, H. 2018 Effects of activation energy on the instability of oblique detonation surfaces with a one-step chemistry model. *Phys. Fluids* **30**, 106110.